

A comparative study of shear wave speed estimation techniques in optical coherence elastography applications.

Fernando Zvietcovich^{*a}, Jianing Yao^b, Ying-Ju Chu^c, Panomsak Meemon^d, Jannick P. Rolland^b, Kevin J. Parker^{a,c}

^aDepartment of Electrical and Computer Engineering, University of Rochester, Rochester, NY, USA 14627; ^bThe Institute of Optics, University of Rochester, Rochester, NY, USA 14627; ^cDepartment of Biomedical Engineering, University of Rochester, Rochester, NY, USA 14627; ^dSchool of Physics, Institute of Science, Suranaree University of Technology, Nakhon Ratchasima, Thailand 30000

ABSTRACT

Optical Coherence Elastography (OCE) is a widely investigated noninvasive technique for estimating the mechanical properties of tissue. In particular, vibrational OCE methods aim to estimate the shear wave velocity generated by an external stimulus in order to calculate the elastic modulus of tissue. In this study, we compare the performance of five acquisition and processing techniques for estimating the shear wave speed in simulations and experiments using tissue-mimicking phantoms. Accuracy, contrast-to-noise ratio, and resolution are measured for all cases. The first two techniques make the use of one piezoelectric actuator for generating a continuous shear wave propagation (SWP) and a tone-burst propagation (TBP) of 400 Hz over the gelatin phantom. The other techniques make use of one additional actuator located on the opposite side of the region of interest in order to create an interference pattern. When both actuators have the same frequency, a standing wave (SW) pattern is generated. Otherwise, when there is a frequency difference df between both actuators, a crawling wave (CrW) pattern is generated and propagates with less speed than a shear wave, which makes it suitable for being detected by the 2D cross-sectional OCE imaging. If df is not small compared to the operational frequency, the CrW travels faster and a sampled version of it (SCrW) is acquired by the system. Preliminary results suggest that TBP (error < 4.1%) and SWP (error < 6%) techniques are more accurate when compared to mechanical measurement test results.

Keywords: Elastography, vibration OCE, optical coherence tomography, shear waves, comparison, gelatin phantoms.

1. INTRODUCTION

Biomechanical properties of tissue such as elasticity provide important information that can be used to better understand human physiological processes and their interactions. In particular, studies demonstrate that certain pathologies can be characterized by tissue elasticity, e.g., glaucoma¹, breast cancer², liver fibrosis³, etc. Elasticity measurement using the optical coherence tomography (OCT) imaging modality, also called optical coherence elastography (OCE), is able to produce micro-scale resolution elasticity images in the range of 1 mm – 10 mm depth field of view. Therefore, OCE enables the measurement of elastic properties of cells and small scale bio-components compared to other modalities such as ultrasound elastography⁴ (US), and magnetic resonance elastography⁵ (MRE).

This research will focus on the implementation and comparison of dynamic OCE techniques which utilize the propagation of transient or sinusoidal steady state mechanic perturbations in order to quantify elastic properties of tissue. We estimate the speed of shear waves propagating in the sample without any previous knowledge of the loading stress.⁶ Several investigations have been done in this area when mechanical actuators⁷⁻⁹, acoustic radiation force (ARF)^{10,11}, and air-puff excitation^{12,13} are utilized in the wave generation. In particular, Manapuram et al.⁷ used a swept-source OCT for measuring shear wave pulse speed in gelatin phantoms. Song et al.⁸ proved that a phase-sensitive OCT system can be used for tracking mechanical waves in gelatin samples at a frame rate of 47 kHz. Meemon et al.⁹ studied the measurements of elasticity in gelatin phantoms by tracking the speed of a steady state interference pattern (crawling wave) produced by two harmonic sources.

*fzvietco@ur.rochester.edu; phone 1 585 275-5069

Similarly, ARF enables the generation of shear waves in tissue. Song et al.¹¹ induced shear waves using a 128 elements linear array ultrasound imaging transducer and measured its phase speed in order to generate elasticity maps in tissue-mimicking phantoms. Finally, the use of an air puff excitation to produce surface waves in tissue was successfully demonstrated by Wang, et al.¹³ In their research, the depth-dependent phase velocity of Lamb waves was estimated in *ex vivo* rabbit cornea in order to distinguish four biomechanically distinct layers.

The present study aims to compare five different dynamic OCE techniques for estimating elastic properties in simulations (numerical analysis) and experiments (gelatin tissue-mimicking phantoms). We combine the effect of one single source and two sources of harmonic vibration for generating wave patterns with different properties. The first two techniques make the use of one piezoelectric actuator to produce a continuous shear wave propagation, and a tone-burst propagation of 400 Hz over the gelatin phantom. The remaining techniques make use of one additional actuator located on the opposite side of the region of interest (ROI) in order to create an interference pattern with certain properties which enables the wave speed estimation. For all methods, the shear wave speed is estimated in both sides of the gelatin phantom. Accuracy, contrast-to-noise ratio (CNR), and resolution are measured and compared.

2. METHODS

2.1 Phantom preparation

A two-sided gelatin phantom was prepared by using 10% and 15% gelatin concentration in each side in order to ensure differentiated mechanical properties (Young's modulus). Light scatterers were provided to the phantom by adding 2% concentration of intralipid powder. The shape of the phantom is a rectangular cuboid of dimensions 15 x 7 x 3 cm (Figure 1a) and its refractive index is approximately 1.35 which is close to real tissue.

The Young's modulus of each side of the phantom was measured by conducting a stress-relaxation compressive test in three samples ($n = 3$) of each concentration using a MTS Q-Test/5 Universal Testing Machine (MTS, Eden Prairie, Minnesota, USA) with a 50 N load cell using a compression rate of 0.5 mm/s, a strain value of 5%, and total measurement time of 600 s. A fractional derivative standard linear solid (FD-SLS) model¹⁴ was used to fit the stress-time plots in order to obtain frequency dependent Young's modulus. Finally, assuming an incompressible (Poisson's ratio of 0.5), homogenous and isotropic medium, the calculated Young's modulus (E) is related to the shear wave speed (v_{shear}) by

$$v_{shear} = \sqrt{\frac{E}{3\rho}} \quad (1)$$

where ρ is the mass density. The shear wave speed for each side of the phantom is estimated and used as a ground truth measurement during the comparison.

2.2 Experimental setup

A phase-sensitive optical coherence tomography (PhS-OCT) is implemented on a swept-source OCT system (HSL-2100-WR, Santec, Aichi, Japan) with a center wavelength of 1,318 nm and a full-width half-maximum (FWHM) bandwidth of 125 nm. The imaging depth was measured to be 5 mm (-10 dB sensitive fall-off). The optical lateral resolution is approximately 20 μm , and the FWHM of the axial point spread function after dispersion compensation is 10 μm . A galvo-scanner was used to change the lateral position of the beam in the sample. The synchronized control of the galvo-scanner and the OCT data acquisition was conducted through a LabView (Version 14.0f1, National Instruments Corporation, Austin, TX, USA) platform connected to a work station.

The separation between the phantom surface and the beam source is approximately 9 cm. Two piezoelectric actuators (APC 40-2020, APC International, Ltd., Macheysville, PA, USA) were located on each side of the phantom as shown in Figure 1b. These actuators were connected to stereo amplifiers (LP-2020A+, Lepai, Houston, Texas, USA) that receive harmonic signals from dual channel function generator (AFG320, Tektronix, Beaverton, OR, USA). The maximum lateral field of view of the ROI in the phantom is 30 mm and the maximum depth is 2.5 mm. Both actuators were located approximately 8 cm from the center of the region of interest (ROI) (Figure 1b). The excitation frequency, acquisition protocol, and use of one or two vibration sources will depend on the OCE method.

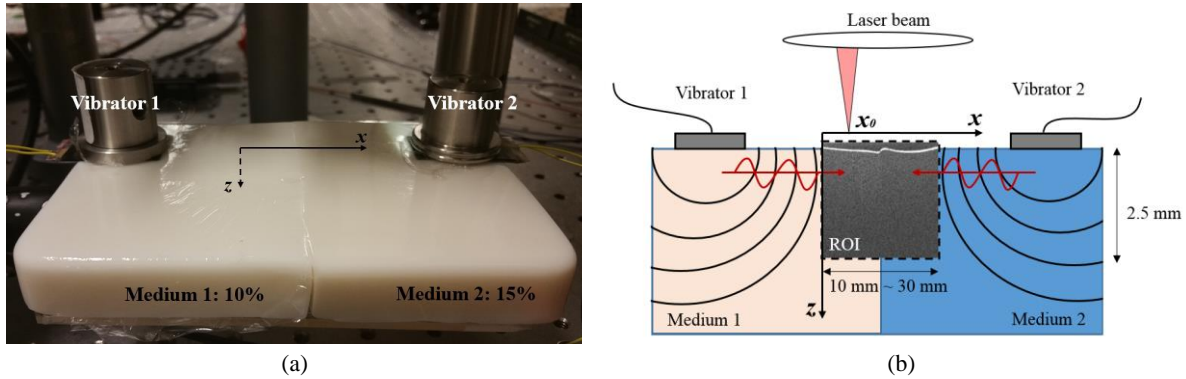


Figure 1 (a) Two-sided gelatin phantom (10%, 15% gel concentration each side). (b) Experimental setup showing a cross section of the phantom, location of vibrators, region of interest, and dimensions.

2.3 Crawling wave (CrW) method

This method was initially proposed in ultrasound elastography¹⁵, and then applied in OCE as reported by Meemon et al.⁹ Here, two harmonic actuators generate shear waves W_{left} and W_{right} propagating one against the other at frequencies $f_{left} = 400$ Hz and $f_{right} = 400.4$ Hz ($\Delta f = 0.4$ Hz), respectively. According to Wu, et al.¹⁵, an interference wave (crawling wave) is generated out of the interaction of these two initial waves, and it propagates with speed v_{CrW} given by

$$v_{CrW} = v_{shear} \frac{\Delta f}{2f + \Delta f} \quad (2)$$

where f is frequency of the first wave, $\Delta f = f_{right} - f_{left}$ is the frequency difference between both waves, and v_{shear} is the shear wave speed of any wave in the medium. Since Δf can be controlled to be $\Delta f \ll f$, we can make the crawling wave speed v_{CrW} slow enough to be detected by scanning multiple B-mode motion frames at a frame rate of 5 frames/s. Each frame is formed by 1500 A-lines covering a lateral field of view of the ROI of 10 mm (lateral sampling resolution of $6.6 \mu\text{m}$) as described in Figure 2. A total of 200 frames were acquired. Finally, the shear wave speed can be estimated based on the crawling wave speed by using the phase derivative method described by Meemon et al.⁹ in which the local wave number $k(x)$ of the shear wave is calculated and plugged in

$$v_{shear}(x) = \frac{2\pi f}{k(x)} \quad (3)$$

where $v_{shear}(x)$ is the shear wave speed at a given lateral position.

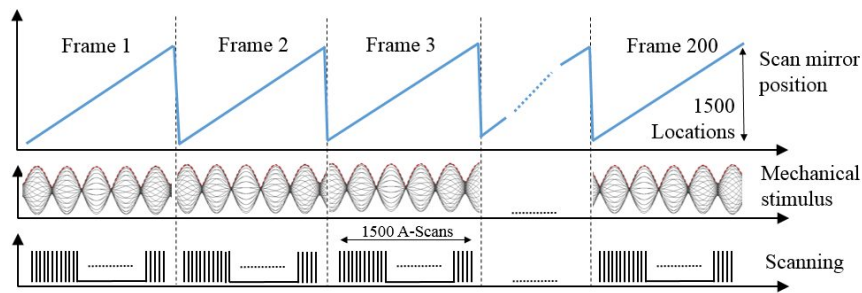


Figure 2 CrW acquisition protocol using a SS-OCT system.

2.4 Swept crawling wave (SCrW) method

This method is analogous to the CrW method, however the relation $\Delta f \ll f$ is no longer required. In this case, the CrW speed is much higher and the benefits of detecting the slow wave without aliasing are not possible. However, if sampling theory is applied to acquisition process, a mathematical model can be found in order to recover the shear wave velocity. The acquisition protocol is based on the formation of M-mode maps for each lateral position; that is, for a given lateral location x_0 , M depth A-lines are acquired at a rate of 20 kHz (time resolution of $50 \mu\text{s}$) as shown in Figure 3. Subsequently, the galvo-scanner redirects the laser beam to the next lateral location x_1 . The M-scanning is performed consecutively for each position x_n until the entire field of view of 30 mm is scanned. It should be noted that while the scanning process takes place, the crawling wave is propagating simultaneously.

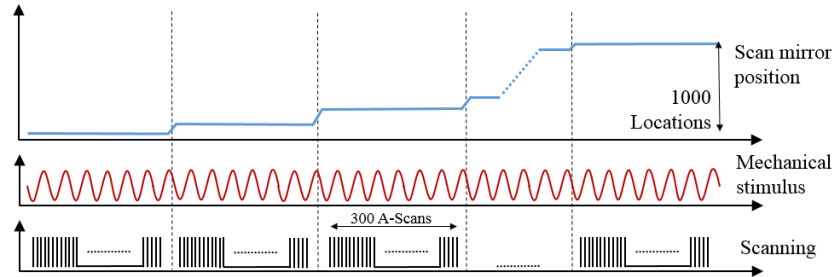


Figure 3 Acquisition protocol of SCrW, SWP, and SW methods using a PhS-OCT system.

It can be demonstrated that the spatial wave number of the interference pattern (k_{SCrW}) detected is related to the spatial wave number of the shear wave ($k(x)$) in the medium as follows:

$$k_{SCrW}(x) \approx 2\pi\Delta f \frac{\Delta_t}{\Delta_x} + 2(k(x)) \quad (4)$$

where Δ_t is the lag time calculated as the sum of the time taken by the system to acquire $M = 300$ A-lines (15 ms) plus the time taken by galvo-scanner to redirect the laser beam (5 ms), and Δ_x is the lateral sampling resolution. For the acquisition of $N = 1000$ A-lines covering the lateral ROI, then $\Delta_x = 30 \mu\text{m}$, and $\Delta_t = 20 \text{ms}$. Equation 4 enables the recovery of $k(x)$ (needed for estimating the local shear wave speed) based on $k_{SCrW}(x)$ using two estimators: local fitting and Hoyt's algorithm¹⁶. The local fitting estimator fits a portion of the scanned SCrW signal with a sinusoidal model in order to retrieve local values of the wave number $k_{SCrW}(x)$. The Hoyt's estimator converts the SCrW signal into a complex-valued signal using a Hilbert transform and then, applies complex cross-correlation in order to estimate $k_{SCrW}(x)$.

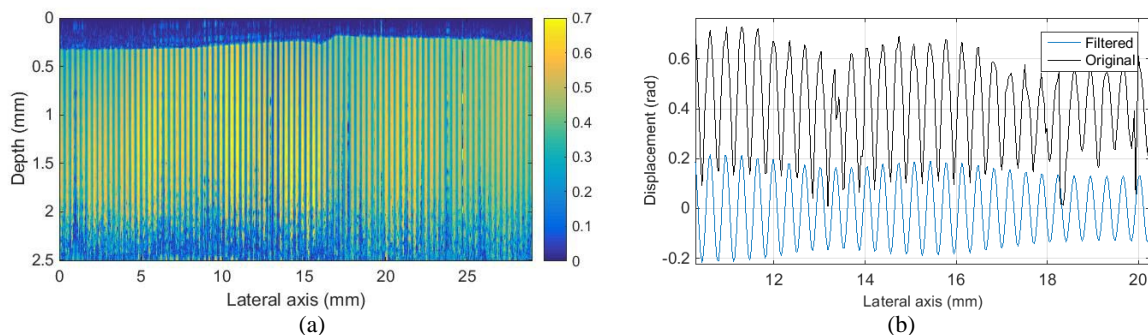


Figure 4 (a) Amplitude map generated using the SCrW method. (b) Profile section of (a) showing the unfiltered and filtered versions.

Figure 4a illustrates the 2D version of the SCrW harmonic signal. Since $k_{SCrW}(x) > k(x)$, there are more harmonic cycles along the lateral axis, which may improve the calculation of $k(x)$ by using Hoyt's estimator and local fitting. Figure 4b depicts a 1D profile of the 2D map as well as its filtered version. Once $k(x)$ is obtained, the shear wave speed is calculated using Equation 3.

2.5 Standing wave (SW) method

In this method, both harmonic vibrators have the same frequency using the setup configuration in Figure 1b, that is, $\Delta f = 0$. Then, $v_{CrW} = 0$, and the CrW pattern becomes a standing wave (SW). The shear wave speed estimation then reduces to the estimation of $k(x)$ in the standing wave pattern as described by Equation 3. As in the SCrW case, $k(x)$ can be recovered by applying Hoyt's estimator¹⁶ to the previous signal. However, it is important to note that the number of cycles of the SW signal will be much less than the SCrW case, which will decrease the accuracy in the estimation. Figure 5a illustrates the 2D version of the harmonic SW signal. It is evident that the wave number decreases from the left to the right side of the image, which proves the relationship between $k(x)$ and the shear wave speed. A 1D profile version of the 2D SW signal is shown in Figure 5b.

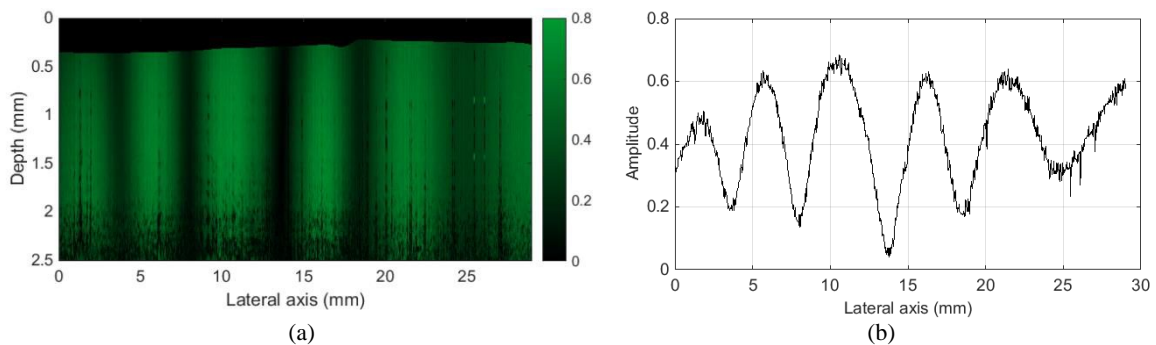


Figure 5 (a) Amplitude map generated using the SW method. (b) Profile extracted from (a).

2.6 Shear wave propagation (SWP) method

This method makes use of the left vibration source in the setup shown in Figure 1b. A continuous harmonic wave $W_{left}(x, t)$ is sent through the right direction of the phantom at a frequency of $f = 400$ Hz. The M-mode acquisition approach is used with the same parameters as in the SCrW and SW methods. The main idea is to generate space-time representations of the propagating shear wave for all depths within the ROI. The main difficulty lies in the high speed of the shear wave compared to the acquisition speed. If M-mode scanning is performed in the lateral position x_0 , when the beam moves to the subsequent position x_1 , the shear wave will propagate several cycles adding an unknown phase. This problem is solved by making the acquisition time (Δ_t) in each lateral position a multiple of the periodicity of the shear wave vibration ($T = 1/f$) in order to avoid a time dependent phase. For $\Delta_t = 20$ ms, the synchronization is ensured for a vibration at a frequency of $f = 400$ Hz. Figure 6a represents the space-time map calculated by tracking the movement of the wave along the lateral axis as a function of time at a given depth location. The change of slope (related to the shear wave velocity) from one medium to the other is evident (Figure 6b). Applying the phase derivative method as mentioned in section 2.3, the shear wave speed is computed.

2.7 Tone-burst propagation (TBP) method

TBP is the final method compared in this study. It uses one harmonic source located in the left side to create a tone-burst of a surface acoustic wave (SAW) propagating within the ROI of the phantom. The tone is formed by one cycle of a harmonic wave of $f = 400$ Hz. The M-mode approach is used for generating space-time representations of the propagating pulse as in the SWP method. In this case, there is no communication between the function generator (which produces the tone-burst) and the OCT acquisition system; then, similarly to the SWP method, a synchronization approach is required (Figure 7). A tone is sent each 35 ms, and $M = 1400$ A-lines are scanned in $N = 400$ lateral positions. Then, the system is able to detect at least 2 tones in a single M-mode scanning, which requires 70 ms. The time given to the galvo-scanner for redirecting the beam between consecutive lateral positions is 35 ms in order to ensure the synchronization requirement.

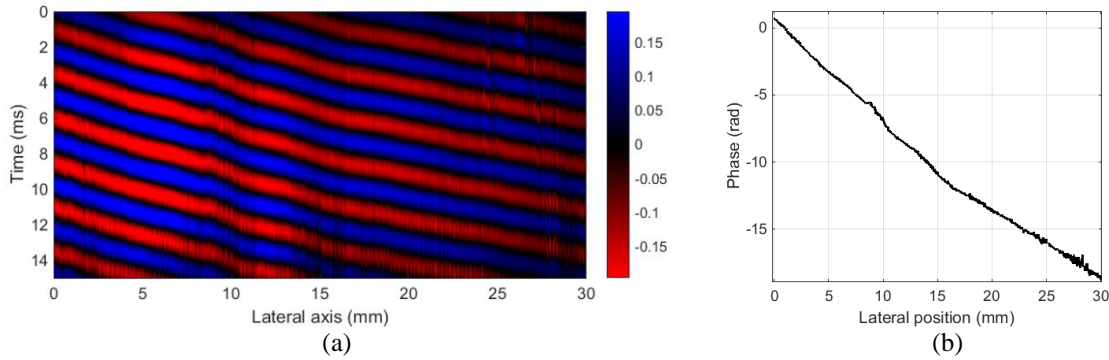


Figure 6 (a) Space-time map describing a shear wave propagation (SWP) taken at a depth of 0.8 mm in the phantom. (b) Profile describing the wave propagation extracted from (a).

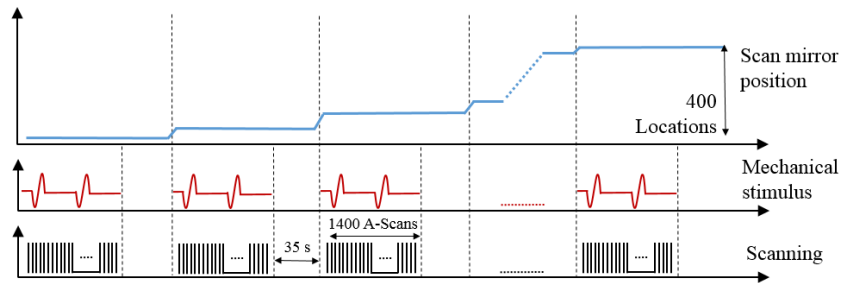


Figure 7 Acquisition protocol of TBP method using a PhS-OCT system.

Four hundred M-mode maps are acquired using the described protocol in order to cover the ROI lateral axis of 30 mm. A 2D M-mode map is formed using 1400 (time axis) x 1024 (depth axis) elements. We rearranged the scanning into a 3D volume of 400 x 1024 x 1400 elements in the lateral, axial, and time axes, respectively. 2D spatial motion frames can be obtained based on the 3D volume at a frame rate of 20 kHz (time resolution 50 μ s). The propagation of the tone-burst can be represented as a 2D profile cut of the 3D volume at a given depth z which will provide a 2D space-time map (Figure 8a). Here, it is evident that the slope of the tone trajectory changes from one medium to the other as shown in Figure 8b. The shear wave speed can be estimated by calculating the local slope of the pulse trajectory as

$$v_{shear} = \frac{\Delta d_{shear}}{\Delta t_{shear}} \quad (5)$$

where Δd_{shear} is the propagated distance of a transient shear wave tone during time Δt_{shear} . This estimation technique is also called the time-of-flight (ToF) and is widely used in ultrasound and OCT elastography.¹⁷ In addition, surface acoustic waves (SAW) are produced when a vibration is generated in a solid-vacuum interface.¹⁸ Since the penetration depth of an OCT system typically ranges some millimeters from the interface, Rayleigh waves are more likely to be scanned than shear waves. Then, for a linear isotropic medium with a Poisson's ratio $\nu = 0.5$, a correction needs to be added as described by

$$v_{shear} \approx 1.05 * v_{Rayleigh} \quad (6)$$

For further details about Rayleigh wave properties, we refer the reader to Viktorov¹⁸.

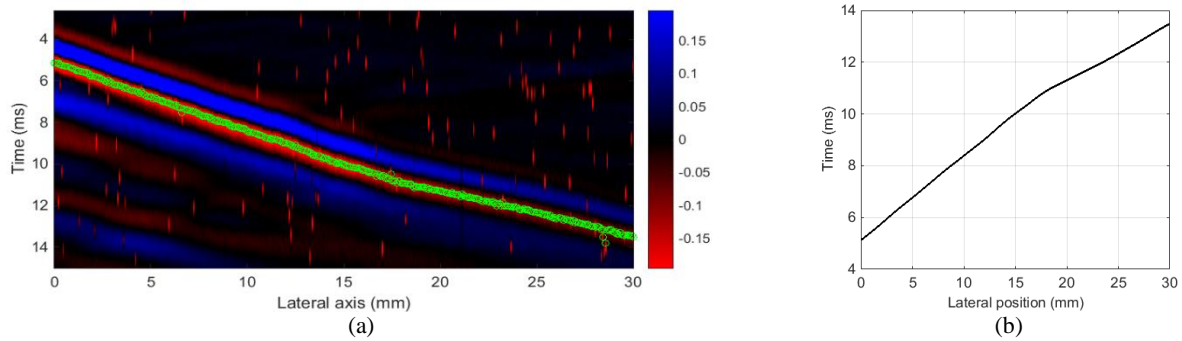


Figure 8 (a) Space-time map extracted from the wave propagation using the TBP method taken at a depth of 0.8 mm in the phantom. (b) Propagation profile extracted from (a).

2.8 Numerical simulations

All OCE methods were tested in a numerical wave field simulation using the k-space method conducted in the k-Wave toolbox for MATLAB (The Mathworks Inc, Natick, MA, USA) recreating the same mechanical properties and dimensions of the phantom, vibration sources, boundary conditions and ROI. A two-sided media was defined with a corresponding shear wave speed of $c_s^1 = 3.11$ m/s, and $c_s^2 = 4.78$ m/s. The size of the 2D grid was 78 mm (600 elements) x 43 mm (300 elements) in the lateral and axial directions, respectively. The two vibration sources introduce axial up-and-down particle velocity in the medium in order to generate approximately planar shear waves propagating in the lateral direction. Spatial-resolved particle velocity output was stored and, subsequently, processed according to the selected OCE method.

3. RESULTS

3.1 Mechanical measurements

Stress relaxation curves obtained with the compression test were fitted using a four-parameter FD-SLS model by using a non-linear constrained optimization approach for both phantom concentrations. Subsequently, shear wave speed versus excitation frequency plots were obtained by using the calculated parameters and a Fourier domain relationship described in Schmidt, et al.¹⁴ We found that the shear wave velocities of the 10%, and 15% gelatin phantoms for a 400 Hz excitation are 3.11 ± 0.05 m/s, and 4.78 ± 0.06 m/s, respectively.

3.2 Simulation and experimental results

Shear-wave-speed maps (SWSM) that represent the 2D shear wave speed for each lateral and depth position in a color-coded fashion were obtained by using numerical simulation for all methods proposed in this study: CrW, SCrW, SW, SWP, and TBP as shown in Figure 9. For each case, a mean-speed lateral profile was calculated in order to visualize the speed transition from the 10% to the 15% medium. Simulations were performed under zero mean white Gaussian noise (SNR 24dB) in order to recreate similar conditions during experiments. We evaluated accuracy, precision of shear wave speed, lateral resolution R_{2080} , and CNR as shown in Table 1. The ground truth speed values were defined in the setup of the simulation described in section 2.8.

Spatial lateral resolution R_{2080} is defined as the distance from 20% to 80% of the shear speed transition from one medium to the other. It provides important information about the effectiveness of differentiating elastic properties of small elements by means of a sigmoid function fitted to the estimated shear wave speed profile as described by Rouze, et al.¹⁹ The contrast to noise ratio (CNR) parameter provides information regarding contrast between the two shear wave speed regions (the 10% and 15% concentration regions of the phantom) in the presence of noise related to the OCE method. The CNR is given by

$$CNR = \frac{|\mu_{15\%} - \mu_{10\%}|}{\sqrt{\sigma_{15\%}^2 + \sigma_{10\%}^2}} \quad (7)$$

where $\mu_{10\%}$, $\mu_{15\%}$ are the mean values of shear wave speed, and $\sigma_{10\%}$, $\sigma_{15\%}$ are their standard deviation calculated within a selected region in the 10% and 15% regions, respectively.

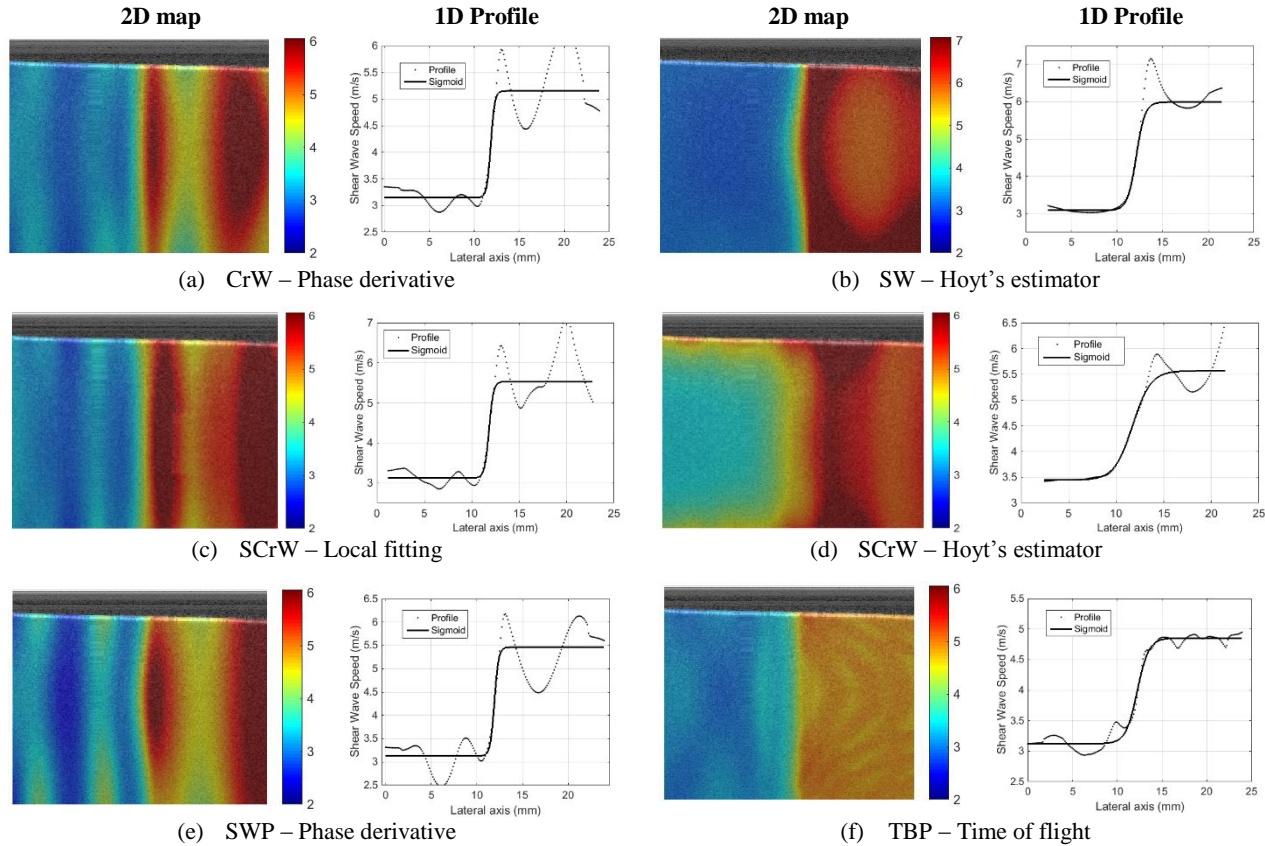


Figure 9 Space-resolved 2D shear wave maps and 1D profiles for all techniques: CrW, SW, SCrW, SWP, and TBP obtained from numerical simulations.

Table 1 Accuracy and precision error of shear wave speed, contrast to noise ratio (CNR), and resolution (R_{2080}), for all methods extracted from numerical simulations under Gaussian noise corruption (SNR 24dB). PhD = phase derivative estimator; Hoyt = Hoyt's estimator; ToF = time of flight approach.

Method		Gel 10%		Gel 15%		CNR	R_{2080} (mm)
		Accuracy error	Precision error	Accuracy error	Precision error		
CrW	PhD	0.74%	6.27%	11.67%	14.39%	3.12	0.73
	Fitting	0.22%	7.43%	13.79%	18.18%	2.55	0.55
SCrW	Hoyt	11.22%	11.03%	14.38%	19.47%	1.85	4.29
SW	Hoyt	1.88%	1.10%	31.77%	3.36%	16.34	1.34
SWP	PhD	3.55%	2.47%	15.80%	2.10%	18.78	0.69
TBP	ToF	0.90%	3.76%	1.36%	1.35%	16.16	1.20

Mean-speed lateral profiles were obtained in experiments with phantoms in order to visualize the speed transition from the 10% to the 15% medium. The accuracy and precision error were calculated within a region in each side of the profile. The mechanical measurement (MM) results were used as the ground truth for all methods. Preliminary experimental results report that the TBP method (accuracy error < 4.1%) and SWP method (accuracy error < 6%) are the most accurate OCE methods compared to all techniques, as reported in Table 2. Figure 10 shows the sigmoid function after being fitted to the actual shear wave speed profiles for the TBP and SWP methods. R_{2080} and CNR are also calculated and shown in Table 2. The axial resolution of speed profiles is the same for all techniques and is equal to the axial sampling resolution of the B-mode OCT images ($2.5 \mu\text{m}$).

Table 2 Accuracy and precision error of shear wave speed estimation, contrast to noise ratio (CNR), and resolution (R_{2080}), for all methods extracted from experimental results.

	Gel 10%		Gel 15%		CNR	R_{2080} (mm)
	Accuracy error	Precision error	Accuracy error	Precision error		
CrW	12.08%	4.30%	1.51%	3.91%	5.66	0.99
SCrW	24.14%	9.70%	11.89%	11.53%	2.06	1.36
SW	24.81%	13.42%	37.30%	16.10%	2.28	1.30
SWP	5.98%	9.10%	4.59%	2.82%	5.14	0.82
TBP	0.23%	6.77%	4.08%	7.15%	3.81	0.88

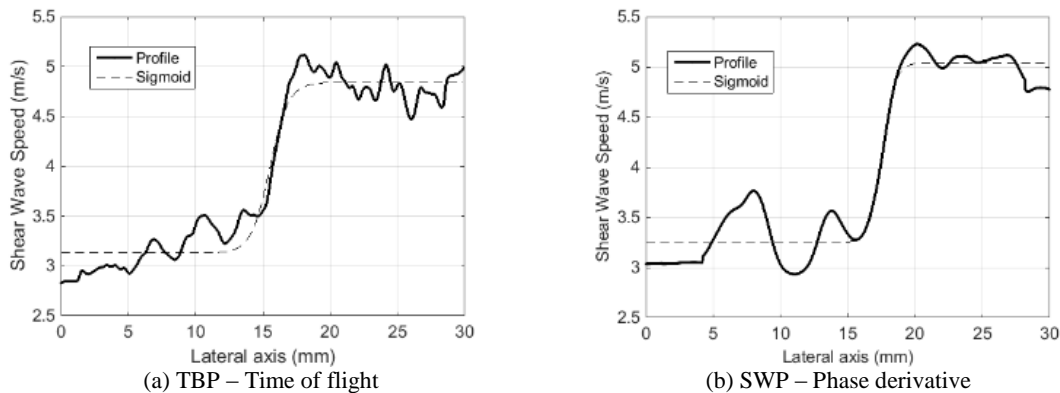


Figure 10 Shear wave speed profiles using (a) TBP method, and (b) SWP method obtained from experiments in a two-sided gelatin phantom.

4. DISCUSSIONS AND CONCLUSIONS

Five OCE methods were evaluated in the estimation of shear wave speed in simulations (numerical analysis) and experiments (two-sided gelatin tissue-mimicking phantom of 10% and 15% concentration). As shown in Table 1, numerical results predicts that the TBP method has the most accurate speed estimation in both sides of the phantom (accuracy error < 1.5%) for the same noise conditions. This outcome is then confirmed by experimental results as reported in Table 2 for the TBP method (accuracy error < 4.1%). SWP has the second most accurate results (accuracy error < 6%) in experiments, and it also provides the second best CNR. The remaining methods overestimate the shear wave speed in both sides of the phantom in simulation and experiments. There is a marked difference between OCE methods that use one vs. two wave vibration sources. TBP and SWP remain more accurate than CrW, SCrW, and SW. This behavior is attributed to the multiple wave reflections in all boundaries of the phantom that are more prevalent in the dual source and steady state techniques. OCE methods using two sources have twice the number of reflections than one-source methods in experiments.

TBP is less sensitive to reflections than all other methods because the energy of the propagating pulse decays rapidly compared to a continuous wave. However, a shear wave traveling from one medium to another of different elastic modulus produces a reflection that cannot be avoided.

In summary, all five evaluated vibrational OCE methods have both advantages and limitations. In particular, the TBP method reports the best accuracy in both sides of the phantom during experiments and numerical simulations. It is also less sensitive to reflections which make it a promising technique for the quantitative estimation of elasticity in tissue. Future work will be focused on the frequency dependent estimation of shear wave speed in order to calculate the viscosity parameter, which has been demonstrated to be an important biomarker in characterizing tissue such as human liver²⁰, and human cornea²¹.

ACKNOWLEDGEMENTS

The development of instrumentation required for this work was supported by the II-VI Foundation. Fernando Zvietcovich is supported by the Fulbright Program (U.S.A. Department of State), and Fondo para la Innovacion, la Ciencia y la Tecnologia FINCyT (Peruvian Government).

REFERENCES

- [1] Detorakis, E.T. and Pallikaris, I. G., "Ocular rigidity: biomechanical role, in vivo measurements and clinical significance," *Clinical & Experimental Ophthalmology* 41(1), 73-81 (2013).
- [2] Donald, B. P., Jonathan, B., Abbas, S. and Justin, S., "Visualization and quantification of breast cancer biomechanical properties with magnetic resonance elastography," *Physics in Medicine and Biology* 45(6), 1591 (2000).
- [3] Sandrin, L., Fourquet, B., Hasquenoph, J.-M., Yon, S., Fournier, C., Mal, F., Christidis, C., Ziol, M., Poulet, B., Kazemi, F., Beaugrand, M. and Palau, R., "Transient elastography: a new noninvasive method for assessment of hepatic fibrosis," *Ultrasound in Medicine & Biology* 29(12), 1705-1713 (2003).
- [4] Parker, K. J., Doyley, M. M. and Rubens, D. J., "Imaging the elastic properties of tissue: the 20 year perspective," *Physics in Medicine and Biology* 56(1), R1 (2011).
- [5] Muthupillai R., Lomas, D. J., Rossman, P. J., Greenleaf, J. F., Manduca, A. and Ehman, R. L., "Magnetic resonance elastography by direct visualization of propagating acoustic strain waves," *Science* 269(5232), 1854-1857 (1995).
- [6] Li, C., Guan, G., Reif, R., Huang, Z. and Wang, R. K., "Determining elastic properties of skin by measuring surface waves from an impulse mechanical stimulus using phase-sensitive optical coherence tomography," *Journal of The Royal Society Interface* 9(70), 831-841 (2012).
- [7] Manapuram, R., Aglyamov, S., Menodiado, F. M., Mashiatulla, M., Wang, S., Baranov, S. A., Li, J., Emelianov, S. and Larin, K. V., "Estimation of shear wave velocity in gelatin phantoms utilizing PhS-SSOCT," *Laser Phys.* 22(9), 1439-1444 (2012).
- [8] Song, S., Huang, Z. and Wang, R. K., "Tracking mechanical wave propagation within tissue using phase-sensitive optical coherence tomography: motion artifact and its compensation," *Journal of Biomedical Optics* 18(12), 121505-121505 (2013).
- [9] Meemon, P., Yao, J., Chu, Y. J., Zvietcovich, F., Parker, K. J. and Rolland, J. P., "Crawling wave optical coherence elastography," *Optics letters* 41(5), 847-850 (2016).
- [10] Qi, W., Chen, R., Chou, L., Liu, G., Zhang, J., Zhou, Q. and Chen, Z., "Phase-resolved acoustic radiation force optical coherence elastography," *Journal of Biomedical Optics* 17(11), 110505-110505 (2012).
- [11] Song, S., Le, N. M., Wang, R. K. and Huang, Z., "Quantitative shear wave optical coherence elastography (SW-OCE) with acoustic radiation force impulses (ARFI) induced by phase array transducer." *Proc. SPIE* 9327, 93270U-93270U-5 (2015).
- [12] Li, J., Wang, S., Manapuram, R. K., Singh, M., Menodiado, F. M., Aglyamov, S., Emelianov, S., Twa, M. D. and Larin, K. V., "Dynamic optical coherence tomography measurements of elastic wave propagation in tissue-mimicking phantoms and mouse cornea in vivo," *Journal of Biomedical Optics* 18(12), 121503-121503 (2013).

- [13] Wang, S. and Larin, K. V., "Noncontact depth-resolved micro-scale optical coherence elastography of the cornea," *Biomedical Optics Express* 5(11), 3807-3821 (2014).
- [14] Schmidt, A. and Gaul, L., "Experimental Investigation and Numerical Treatment of Viscoelastic Materials," *Proceedings of the International Model Analysis Conference* 3(1), 1557-1566 (2008).
- [15] Wu, Z., Taylor, L. S., Rubens, D. J. and Parker, K. J., "Sonoelastographic imaging of interference patterns for estimation of the shear velocity of homogeneous biomaterials," *Physics in Medicine and Biology* 49(6), 911 (2004).
- [16] Hoyt, K., Castaneda, B. and Parker, K. J., "Two-Dimensional Sonoelastographic Shear Velocity Imaging," *Ultrasound in Medicine & Biology* 34(2), 276-288 (2008).
- [17] Elegbe, E. C. and McAleavey, S. A., "Single Tracking Location Methods Suppress Speckle Noise in Shear Wave Velocity Estimation," *Ultrasonic imaging* 35(2), 109-125 (2013).
- [18] Viktorov, I. A., [Rayleigh and Lamb waves: physical theory and applications], Plenum Press, New York, 1-6 (1967).
- [19] Rouze, N. C., Wang, M. H., Palmeri, M. L. and Nightingale, K. R., "Parameters affecting the resolution and accuracy of 2-D quantitative shear wave images," *Ultrasonics, Ferroelectrics, and Frequency Control, IEEE Transactions on* 59(8), 1729-1740 (2012).
- [20] Nightingale, K. R., Rouze, N. C., Rosenzweig, S. J., Wang, M. H., Abdelmalek, M. F., Guy, C. D. and Palmeri, M. L., "Derivation and analysis of viscoelastic properties in human liver: impact of frequency on fibrosis and steatosis staging," *Ultrasonics, Ferroelectrics, and Frequency Control, IEEE Transactions on* 62(1), 165-175 (2015).
- [21] Lombardo, G., Serrao, S., Rosati, M. and Lombardo, M., "Analysis of the Viscoelastic Properties of the Human Cornea Using Scheimpflug Imaging in Inflation Experiment of Eye Globes," *PLoS ONE* 9(11), e112169 (2014).